The rift to break-up evolution of the Gulf of Aden: Insights from 3D numerical lithospheric-scale modelling

Sascha Brune [a,*], Julia Autin [b]

[a] Helmholtz Centre Potsdam, GFZ German Research Centre for Geosciences Section 2.5, Geodynamic Modelling, Potsdam, Germany
[b] IPGS-UMR 7516, Université de Strasbourg/EOST, CNRS, France

ABSTRACT

The Gulf of Aden provides an ideal setting to study oblique rifting since numerous structural data are available onshore and offshore. Recent surveys showed that the spatio-temporal evolution of the Gulf of Aden rift system is dominated by three fault orientations: displacement-orthogonal (WSW), rift-parallel (WNW) and an intermediate E–W trend. The oldest parts of the rift that are exposed onshore feature displacement-orthogonal and intermediate directions, whereas the subsequently active necking zone involves mainly rift-parallel faults. The final rift phase recorded at the distal margin is characterised by displacement-orthogonal and intermediate fault orientations. We investigate the evolution of the Gulf of Aden from rift initiation to break-up by means of 3D numerical experiments on lithospheric scale. We apply the finite element model SLIM3D which includes realistic, elasto-visco-plastic rheology and a free surface. Despite recent advances, 3D numerical experiments still require relatively coarse resolution so that individual faults are poorly resolved. We address this issue by proposing a simple post-processing method that uses the surface stress-tensor to evaluate stress regime (extensional, strike-slip, compressional) and preferred fault azimuth. The described method is applicable to any geodynamic model and easy to introduce. Our model reproduces the observed fault pattern of the Gulf of Aden and illustrates how multiple fault directions arise from the interaction of local and far-field tectonic stresses in an evolving rift system. The numerical simulations robustly feature intermediate faults during the initial rift phase, followed by rift-parallel normal faulting at the rift flanks and strike-slip faults in the central part of the rift system. Upon break-up, displacement-orthogonal as well as intermediate faults occur. This study corroborates and extends findings from previous analogue experiments of oblique rifting on lithospheric scale and allows new insights in the timing of fault successions of the Gulf of Aden and continental rifts in general.

© 2013 Elsevier B.V. All rights reserved.

1. Introduction

By nature, oblique rifts need to be studied in three dimensions and their understanding depends on the ability to reproduce 3D processes. The Tertiary Gulf of Aden is an ideal area to study oblique rifting. The direction of extension is N025°E but the rift has a N075°E-trend (Fig. 1), resulting in a moderately oblique rift system. The fault pattern is well expressed on the present-day conjugate margins. Moreover, the oceanic basin is young (17.6 My), so the sedimentary cover is thin and the conjugate margins are easily correlated.

The Gulf of Aden rift system formed 34–33 My ago and was active until 20 My ago when break-up took place (Leroy et al., 2012). The Gulf of Aden displays a high degree of segmentation with large fracture zones that delimit three distinct segments (Eastern, Central, and Western Segment, Fig. 1a): The Eastern Gulf of Aden features extremely thin transitional crust at the Ocean–Continent Transition (OCT) (Leroy et al.,

2010; Watremez et al., 2011), which most likely involves exhumed serpentinised mantle rocks indicating a magma-poor setting (Leroy et al., 2012). In both the Eastern and the Central Gulf of Aden, margins are thought to be magma-poor as no magmatic structures, such as seaward-dipping reflectors, were recognised in the OCT (e.g. Bosworth et al., 2005). In the Western Gulf of Aden, the margins display volcanic characteristics related to the activity of the Afar hot spot.

Previously, the structural pattern of the Gulf of Aden has been elucidated thanks to field and seismic studies that were conducted onshore and offshore in Oman (Bellahsen et al., 2006; d'Acremont et al., 2005; Fournier et al., 2004) and in Yemen (Huchon and Khanbari, 2003). They allow us to recognise three general fault populations (i) displacement-normal with a fault azimuth of N115°E, (ii) rift-parallel with N075°E and (iii) an orientation that is intermediate between the two former directions (N095°E). The inversion of fault slip data sets permitted the computation of stress tensors corresponding to several local directions of extension (N025°E, N160°E and N–S) in Oman (Bellahsen et al., 2006; Fournier et al., 2004; Lepvrier et al., 2002), in Yemen (Huchon and Khanbari, 2003; Huchon et al., 1991) and at Socotra Island (Fournier et al., 2007). Offshore, near the OCT,

* Corresponding author. Now at: EarthByte Group, School of Geosciences, University of Sydney, Australia. Tel.: +49 331 2881928; fax: +49 331 288 1938.
E-mail address: brune@gfz-potsdam.de (S. Brune).
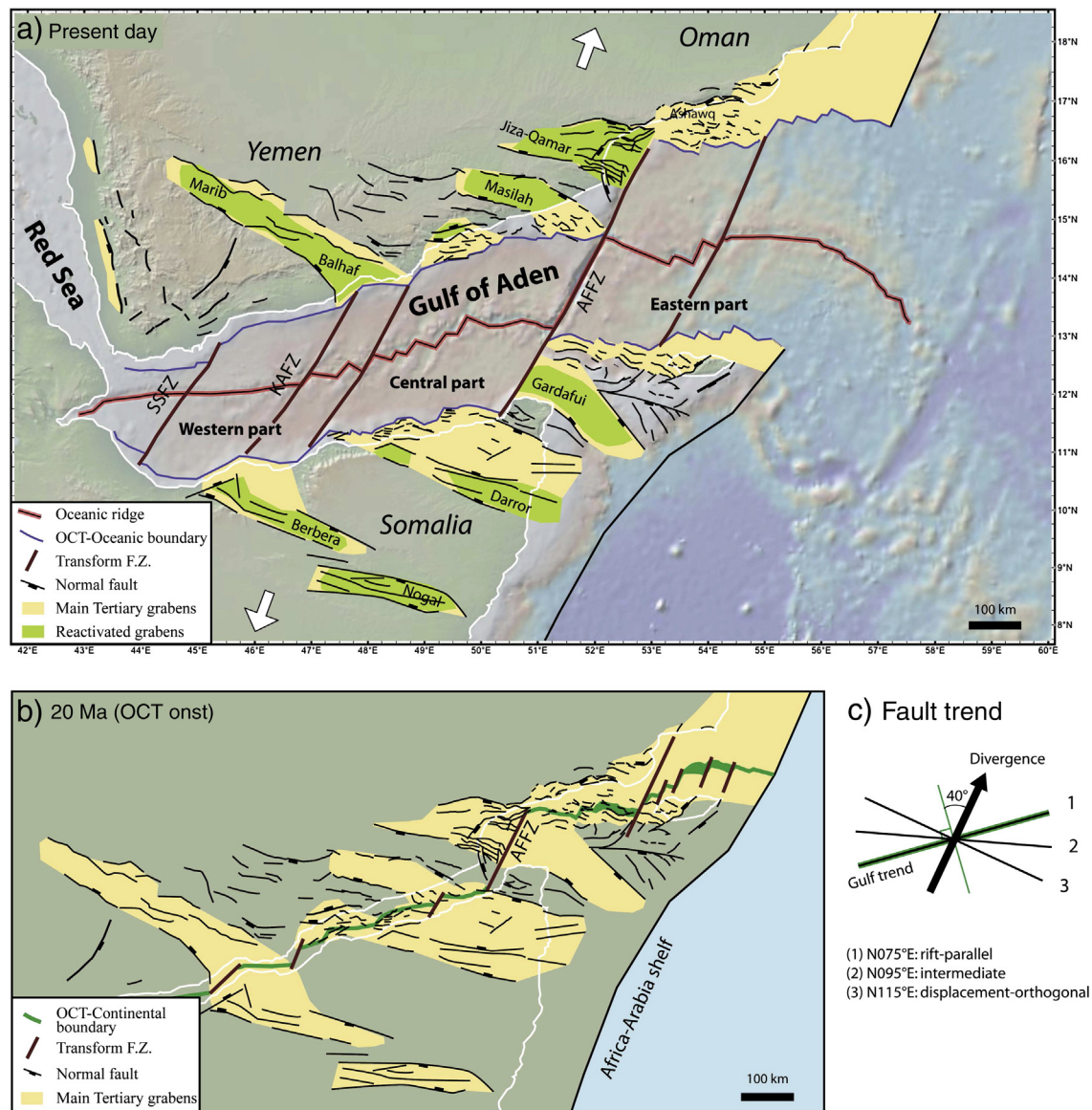
Fig. 1. Gulf of Aden overview map. (a) Structural map of the Gulf of Aden with main Tertiary depocentres and Mesozoic inherited basins (after Bellahsen et al., this volume and Leroy et al., 2012). SSFZ: Shukra El Sheik Fracture Zone, KAFZ: Khanshir Al Irquah Fracture Zone, AFFZ: Alula-Fartak Fracture Zone. (b) Reconstruction of the margins at the onset of the Ocean–Continent Transition (OCT) based on Leroy et al., 2012. (c) Major fault trends observed in the Gulf of Aden.

both the faults and basins mainly strike perpendicular to the Gulf of Aden opening direction (d'Acremont et al., 2005). Bellahsen et al. (this volume) observe that the proximal parts of the margins display intermediate and displacement-orthogonal faults, whereas the OCT displays rift-parallel or displacement-orthogonal faults. The oceanic ridge is orthogonal to the divergence (Dauteuil et al., 2001; Hébert et al., 2001; Tamsett and Searle, 1988). The overall pattern of deformation in the Gulf of Aden shows en-echelon Tertiary sigmoid grabens. This structuration could be linked to Mesozoic inheritance which consists in elongated E–W grabens (Fig. 1b). Previous analogue models of the Arabian plate tend to demonstrate that the obliquity of the Gulf of Aden arises from the interaction between the laterally-evolving subduction of the Tethyan Ocean toward the north and the Afar hot spot in the south-west (Bellahsen et al., 2003).

Fault patterns of oblique rifts have been investigated during the last decades using analogue models on two different levels of complexity: (i) crustal-scale models simplify the rift system to a deforming crust influenced by a basal zone of extension that involves an oblique velocity discontinuity (Clifton et al., 2000; Corti, 2004; Corti et al., 2001, 2003; Mart and Dauteuil, 2000; McClay and White, 1995; Sokoutis et al.,

2007; Tron and Brun, 1991; Withjack and Jamison, 1986). The advantage of this setup is that crustal strain patterns can be studied independently of mantle deformation, but this also limits the applicability to the first rift stage where isostatic balancing with the mantle and lithospheric necking can be neglected. Furthermore, the role of the basal discontinuity is overestimated intrinsically. (ii) Analogue experiments on the lithospheric scale have been conducted recently and successfully reproduced lithospheric thinning and its effect on crustal fault patterns (Agostini et al., 2009; Autin et al., 2010; Sokoutis et al., 2007). However, thermal effects or rheological changes that occur during rifting are not modelled in these experiments and their absence remains a significant limitation of such analogue models. They also do not show the progression from oblique rift initiation to plate rupture.

In contrast to analogue models, state-of-the-art geodynamic codes are capable of computing realistic, temperature-dependent viscosity as well as complex elasto-visco-plastic rheologies. Many numerical models include these features and have been used to study diverse aspects of rift dynamics in two dimensions (e.g. Bassi, 1991; Behn et al., 2002; Braun and Beaumont, 1989; Buck, 1991; Buiter et al., 2008; Burov and Cloetingh, 1997; Huismans and Beaumont, 2003, 2011;

Lavier and Manatschal, 2006; Lavier et al., 2000; Regenauer-Lieb et al., 2006; Rey et al., 2011; van Wijk and Cloetingh, 2002; Zuber and Parmentier, 1986). Despite these advantages, numerical models of oblique rifting intrinsically require computationally expensive calculations in three dimensions. Addressing only the crustal deformation in a rift system strongly limits the computational effort which, in turn, allows for comparatively higher resolution (Allken et al., 2011, 2012; Katzman et al., 1995). However, such models are valid only during the initial rift stage, where the influence of a deforming mantle lithosphere can be neglected. This disadvantage is overcome by numerical experiments that involve both the crust and mantle lithosphere (Dunbar and Sawyer, 1996; Le Pourhiet et al., 2012; van Wijk, 2005; van Wijk and Blackman, 2005). Nevertheless, these models do not account for the weak asthenospheric rheology which becomes influential during late rift stages and continental break-up. Recently, 3D thermo-mechanical rift models that feature crust, lithospheric mantle and asthenospheric mantle have been published: Gac and Geoffroy (2009) investigated the influence of weak, melt-related soft points within an extending lithosphere. They showed that the resultant 3D crustal structures agree well with the tectonic segmentation and zig-zag pattern found at volcanic passive margins. Brune et al. (2012) showed by means of a simple analytical model that oblique rifting is energetically preferred over rift-perpendicular extension, which they corroborated by means of lithospheric-scale numerical experiments. This model has been extended in order to investigate the influence of plume-related lithosphere erosion on the dynamics of continental break-up (Brune et al., 2013).

In this paper, we show that lithospheric-scale numerical experiments are capable to reproduce extensional structures from initial rifting to break-up. We thereby apply elasto-visco-plastic rheology with laboratory-based flow laws for temperature/stress-dependent viscosity. We investigate the fault geometries during oblique rifting based on strain-rate and plastic strain patterns. Moreover, we exploit the fact that numerical models provide direct access to the stress tensor at any numerical element, which allows to infer fine-scale fault patterns. We explicitly compare our experiments to previous analogue modelling results and relate them to the present knowledge about the structure of the Gulf of Aden.

2. Model description

2.1. Numerical model: setup and methods

We consider a rectangular Earth segment that consists of a 20 km thick upper crustal layer with a wet quartzite rheology (Gleason and Tullis, 1995), a lower crustal layer of 15 km thickness with granulite properties (Wilks and Carter, 1990), and a 45 km thick layer of strong mantle material with dry olivine rheology (Hirth and Kohlstedt, 2003). We introduce a chemical asthenosphere by applying the flow law of wet (i.e. 500 ppm H/Si) olivine below 90 km depth (Hirth and Kohlstedt, 2003). The thermal lithosphere–asthenosphere boundary (LAB) that is defined here as the 1350 °C isotherm is set to 100 km depth at the start of the model (Fig. 2a,b) The thermal state of the model is initialised as the equilibrium temperature distribution that results from thermal material parameters and the following boundary conditions: the surface temperature is held constant at 0 °C, below 100 km depth the asthenosphere temperature is set to 1350 °C, and lateral boundaries are thermally isolated. A linear seed is introduced in the model centre by elevating the LAB with an amplitude of 20 km in a region of 20 km width as depicted by the 1350 °C isotherm in Fig. 2a. During subsequent model evolution we fix the bottom boundary temperature to 1350 °C. Our simulation domain measures 249 km times 249 km horizontally and 120 km vertically. We thereby use 275,560 cubic elements with a length of 3 km. All rheological and thermal parameters are listed in Table 1. In the following, we refer to this

setup as "standard scenario". Alternative setups where LAB depth and resolution are modified are discussed in Section 3.3.

We define the angle of obliquity α as the angle between the boundary velocity direction and the rift normal. In this study, we use $\alpha = 40°$, which is representative for the obliquity encountered in the Gulf of Aden, where extension direction and rift normal are oriented N025°E and N015°W, respectively. Extensional rates of the Miocene Gulf of Aden rift system are poorly constrained. Here we assume a full extension velocity of 10 mm/yr that is incorporated in our simulations through velocity boundary conditions at the model sides facing in x-direction so that they move symmetrically with 5 mm/yr. The model velocity is equivalent to 10 km/My which results in a maximum extension of 200 km after 20 My model time. The two sides of the model facing in y-direction are connected via periodic boundary conditions which effectively realizes an infinitely long rift zone. The free surface boundary conditions at the upper model face allow self-consistent evolution of topography. At the lower model boundary, isostatic equilibrium is realized by means of the Winkler boundary condition (e.g. Gerya, 2009). During remeshing, the lower boundary surface is reset to 120 km while new numerical markers are introduced that allow for inflow of asthenospheric material through the bottom surface.

We apply the finite element code SLIM3D (Semi-Lagrangian Implicit Model for 3 Dimensions; Popov and Sobolev, 2008) to solve the coupled conservation equations of momentum

$$-\frac{\partial p}{\partial x_i} + \frac{\partial \tau_{ij}}{\partial x_j} + \rho g_i = 0 \tag{1}$$

energy

$$\rho C_p \frac{DT}{Dt} = \frac{\partial}{\partial x_i}\left(\lambda \frac{\partial T}{\partial x_i}\right) + \tau_{ij}\dot{\varepsilon}_{ij} + \rho A \tag{2}$$

and mass

$$\frac{1}{K}\frac{Dp}{Dt} - \alpha_T \frac{DT}{Dt} + \frac{\partial v_i}{\partial x_i} = 0 \tag{3}$$

with coordinates x_i, time t, material time derivative D/Dt, velocities v_i, temperature T, pressure p, stress deviator τ_{ij}, strain rate deviator $\dot{\varepsilon}_{ij}$, density ρ, gravity vector g_i, heat capacity C_p, heat conductivity λ, thermal expansivity α_T, radioactive heat production A, and bulk modulus K. The Einstein summation rule applies for repeated indices.

Mechanical material properties are introduced by decomposing the deviatoric strain rate tensor into an elastic, viscous, and plastic component (Simo and Hughes, 2000)

$$\dot{\varepsilon}_{ij} = \dot{\varepsilon}_{ij}^{elastic} + \dot{\varepsilon}_{ij}^{viscous} + \dot{\varepsilon}_{ij}^{plastic} = \frac{1}{2G}\hat{\tau}_{ij} + \frac{1}{2\eta_{eff}}\tau_{ij} + \dot{\gamma}\frac{\partial Q}{\partial \tau_{ij}} \tag{4}$$

with the elastic shear modulus G, the objective stress rate $\hat{\tau}_{ij}$, the effective creep viscosity η_{eff}, the plastic multiplier $\dot{\gamma}$, and the plastic potential function Q.

The effective creep viscosity is computed using the flow laws for diffusion, dislocation, and Peierls creep (Kameyama et al., 1999):

$$\eta_{eff} = \frac{1}{2}\tau_{II}\left(\dot{\varepsilon}_{Diff} + \dot{\varepsilon}_{Disloc} + \dot{\varepsilon}_{Peierls}\right)^{-1} \tag{5}$$

where τ_{II} denotes the second invariant of deviatoric stress. Individual flow law formulations are:

Diffusion creep

$$\dot{\varepsilon}_{Diff} = B_{Diff}\tau_{II} \quad \exp\left(-\frac{E_{Diff} + pV_{Diff}}{RT}\right) \tag{6}$$

a **Initial and boundary conditions**

b **Standard setup (Fig. 3&4)**

c **Thin lithosphere (Fig. 5)**

d **Thick lithosphere (Fig. 6)**

e **Analog model (Fig. 8)**
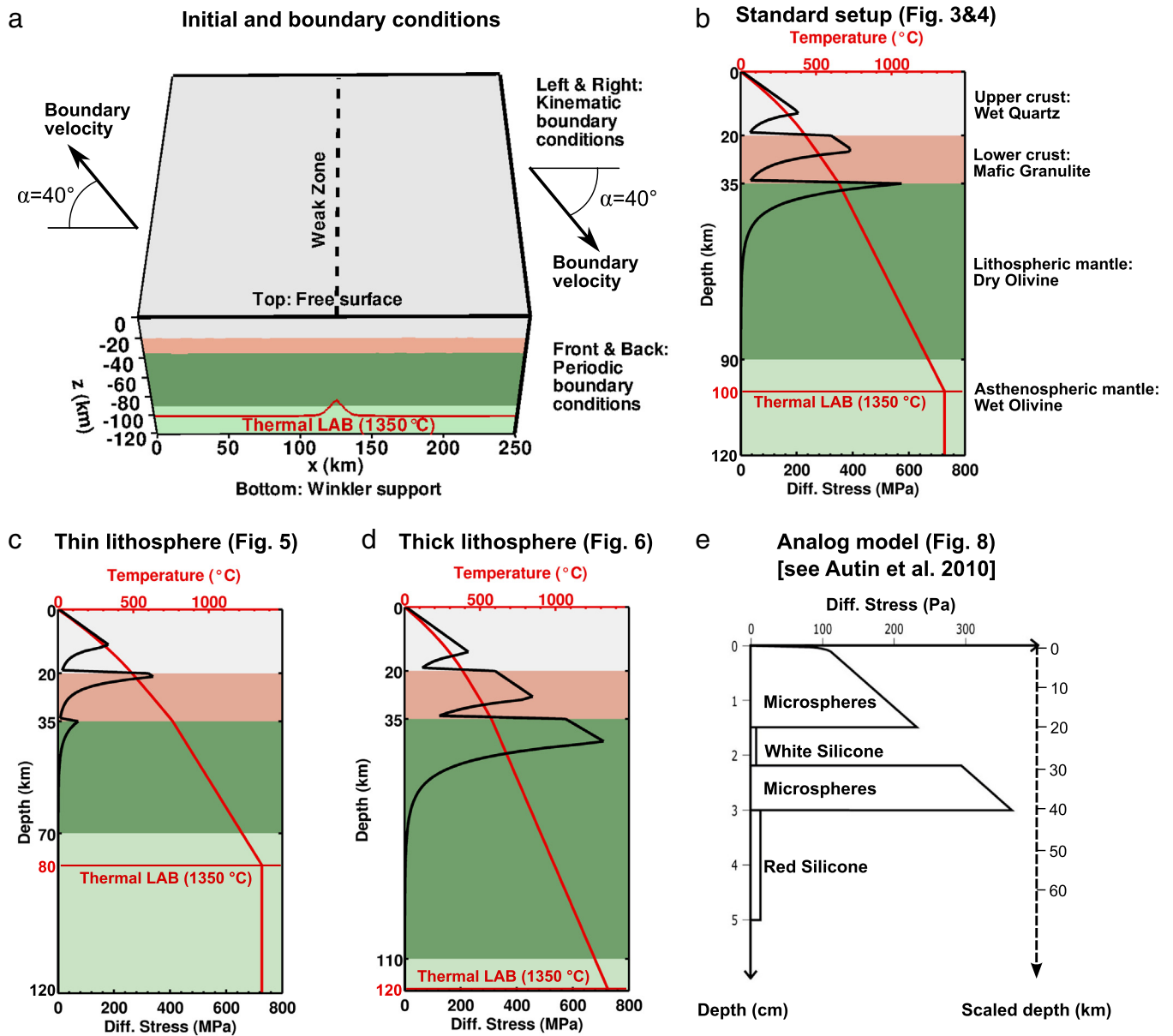**[see Autin et al. 2010]**

Fig. 2. Model setup. (a) Boundary conditions: Extensional velocities are prescribed at the boundaries in x-direction. The angle of obliquity α is defined as the angular difference between extension velocity and rift normal. Periodic boundary conditions in y-direction realize an in principle infinitely long rift zone. Starting conditions: Initially, the system is in thermal equilibrium defined by thermal material parameters as well as surface and asthenosphere temperature (0 °C and 1350 °C respectively). The thermal lithosphere–asthenosphere boundary (LAB) is situated at 100 km depth and is modified by a linear seed in the model centre. (b–c) The thickness of the material layers and the LAB depth define both the temperature and stress distribution at model start. (e) Initial yield strength profile of the analogue model (Autin et al., 2010).

Dislocation creep

$$\dot{\varepsilon}_{Disloc} = B_{Disloc}(\tau_{II})^n \quad \exp\left(-\frac{E_{Disloc} + pV_{Disloc}}{RT}\right) \qquad (7)$$

Peierls creep

$$\dot{\varepsilon}_{Peierls} = B_{Peierls} \quad \exp\left[\frac{-E_{Peierls}}{RT}(1-\beta)^2\right]\left[\frac{\tau_{II}}{\beta\tau_{Peierls}}\right]^{\left(2\beta(1-\beta)\frac{E_{Peierls}}{RT}\right)}. \qquad (8)$$

The Mohr–Coulomb model is used for implementation of plastic failure:

$$F = \frac{1}{2}(\sigma_{max} - \sigma_{min}) + \frac{1}{2}(\sigma_{max} + \sigma_{min})\sin\varphi - c\cos\varphi \leq 0 \qquad (9)$$

with the yield surface F, maximum and minimum principal stresses σ_{max} and σ_{min}, friction angle φ, and cohesion c. All parameter values are explicitly listed in Table 1. Additional information on SLIM3D and its applications can be found in Brune et al. (2012), Brune et al. (2013), Melnick et al. (2012), Popov and Sobolev (2008), Popov et al. (2012), Quinteros and Sobolev (2012), Quinteros and Sobolev (2013), as well as Quinteros et al. (2010).

In many cases oblique rifting arises because inherited lithospheric weak zones like sutures are reactivated with an oblique extensional component (Ziegler and Cloetingh, 2004). We introduce a weak zone by implementing a small linear temperature heterogeneity in the centre of the prospective rift (Fig. 2a). In doing so we anticipate a small amount of lithospheric necking that focuses the extensional deformation into the desired rift axis. This is one possible technique of rift initialization. Alternative means are mechanical anisotropy (Tommasi and Vauchez, 2001), implementation of a weak plastic seed (Huismans and Beaumont, 2003),

Table 1
Model parameters.

Parameter	Upper crust	Lower crust	Strong mantle	Weak mantle
Density, ρ (kg m^{-3})	2700	2850	3300	3300
Thermal expansivity, α_T(10^{-5} K^{-1})	2.7	2.7	3.0	3.0
Bulk modulus, K (GPa)	55	63	122	122
Shear modulus, G (GPa)	36	40	74	74
Heat capacity, C_p(J kg^{-1} K^{-1})	1200	1200	1200	1200
Heat conductivity, λ (W K^{-1} m^{-1})	2.5	2.5	3.3	3.3
Radiogenic heat production, A (μW m^{-3})	1.5	0.2	0	0
Initial friction coefficient, μ (–)	0.6	0.6	0.6	0.6
Maximum plastic friction softening[a]	90%	90%	None	None
Cohesion, c (MPa)	5.0	5.0	5.0	5.0
Pre-exponential constant for diffusion creep, $\log(B_{Diff})$ (Pa^{-1} s^{-1})	–	–	-8.65	-8.65
Activation energy for diffusion creep, E_{Diff} (kJ/mol)	–	–	375	335
Activation volume for diffusion creep, V_{diff} (cm^{-3}/mol)	–	–	6	4
Pre-exponential constant for dislocation creep, $\log(B_{Disloc})$ (Pa^{-n} s^{-1})	-28.0	-21.05	-15.56	-15.05
Power law exponent for dislocation creep, n	4.0	4.2	3.5	3.5
Activation energy for dislocation creep, E_{Disloc} (kJ/mol)	223	445	530	480
Activation volume for dislocation creep, V_{Disloc} (cm^{-3}/mol)	0	0	13	10
Pre-exponential constant for Peierls creep, $\log(B_{Peierls})$ (Pa^{-n} s^{-1})	–	–	11.76	–
Activation energy for Peierls creep, $E_{Peierls}$ (kJ/mol)	–	–	540	–
Peierls stress, $\tau_{Peierls}$ (GPa)	–	–	8.5	–

Dislocation creep parameters for upper crust: wet quartzite (Gleason and Tullis, 1995), lower crust: Pikwitonian granulite (Wilks and Carter, 1990), lithospheric mantle: dry olivine (Hirth and Kohlstedt, 2003), asthenospheric mantle: wet olivine, i.e. 500 ppm H/Si (Hirth and Kohlstedt, 2003). Peierls creep parameters for mantle: (Kameyama et al., 1999).

  [a] The friction coefficient decreases linearly by 90% of the initial value when plastic strain reaches 1, and remains constant for larger strains.

or crustal thickening (van Wijk, 2005). Note that after a small amount of extension, all of these techniques will result in lithospheric necking comparable to our initial condition.

Three weakening mechanisms are reproduced in the model. (i) Friction softening is introduced using a strain-dependent effective friction coefficient that decreases linearly from 0.6 to 0.06 for plastic strains between 0 and 1 while it remains constant at 0.06 for plastic strains larger than 1. (ii) Shear heating results in increased temperature that is proportional to stress multiplied by strain rate. (iii) Dislocation creep intrinsically results in strain rate softening due to the stress exponent $n > 1$ which leads to localised viscosity reduction.

2.2. Stress interpretation method

In most geodynamic codes (including SLIM3D), fault structures are represented by finite width shear bands that localise with a width of several elements. Hence, high-resolution fault patterns that are visible both in nature and in analogue models are difficult to reproduce in relatively coarse 3D models. We address this problem by using a simple post-processing technique that uses the stress tensor at the model surface in order to infer stress regime and the orientation of small-scale faults. This technique extracts additional information from the model which widens the interpretation scope of the numerical experiments.

The stress interpretation method is based on the classic knowledge that all shear stress components are zero at the surface of the Earth, so that one principal stress component has to be oriented vertically which allows to classify the stress regime either as extensional, strike-slip, or compressional (Anderson, 1948). In locally isotropic and homogeneous media, the fault azimuth and fault type (normal, strike-slip, thrust) directly reflect the local stress field. The stress interpretation method operates in two distinct steps: (i) Representing the stress regime at each surface element and (ii) evaluating the optimally oriented fault direction. Both steps are described in detail in the next paragraphs.

2.2.1. Representing the stress regime at each surface element

We visualise the stress regime using the scalar Regime Stress Ratio (RSR) that indicates extension, strike-slip motion and compression on a continuous scale (Buchmann and Connolly, 2007; Hergert and Heidbach, 2011; Simpson, 1997). A similar technique involving the non-dimensional Argand Ratio has been successfully applied to interpret stress states in thin sheet models (England and McKenzie, 1982;

Houseman and England, 1986; Rey and Houseman, 2006). The difference between Argand Ratio and RSR is that the latter is confined to the interval between 0 and 3 which allows direct association of all possible stress regimes as shown in Table 2.

In order to evaluate the RSR value at each surface element, we first compute the principal stress components, i.e. the eigenvalues σ_1, σ_2, and σ_3 of the stress tensor. Together with the corresponding eigenvectors we identify σ_v, σ_h, and σ_H, the vertical, smallest horizontal, and largest horizontal stress component, respectively. Further, we define the index n

$$n = \begin{cases} 0 & if \quad \sigma_h{<}\sigma_H{<}\sigma_v & \text{(normal faulting)} \\ 1 & if \quad \sigma_h{<}\sigma_v{<}\sigma_H & \text{(strike} - \text{slip faulting)} \\ 2 & if \quad \sigma_v{<}\sigma_h{<}\sigma_H & \text{(thrust faulting)} \end{cases}$$

and the ratio R between the smallest and largest differential stress (Bott, 1959).

$$R = \left(\frac{\sigma_2 - \sigma_3}{\sigma_1 - \sigma_3} \right).$$

The RSR value itself is defined as

$$RSR = (n + 0.5) + (-1)^n (R - 0.5)$$

and the physical meaning of this value is listed in Table 2.

2.2.2. Optimal fault orientation

Based on the local stress field, we infer an optimally oriented fault direction at each surface element. Assuming isotropic and homogeneous materials, we follow the standard rules of Andersonian faulting where extensional and compressive stress regimes result in σ_3-orthogonal and σ_1-orthogonal fault azimuths, respectively, while strike-slip faults occur at $\pm\varphi_{eff}$ from σ_1 (with the effective friction angle $\varphi_{eff} = 31°$).

Table 2
Meaning of the Regime Stress Ratio (RSR).

RSR-value:	≤0.5	1	1.5	2	≥2.5
Meaning:	Extension	Transtension	Strike-slip	Transpression	Compression

The RSR value is a scalar value that is continuous between 0 and 3. It is used to infer stress regimes and their associated fault types from stress tensors.
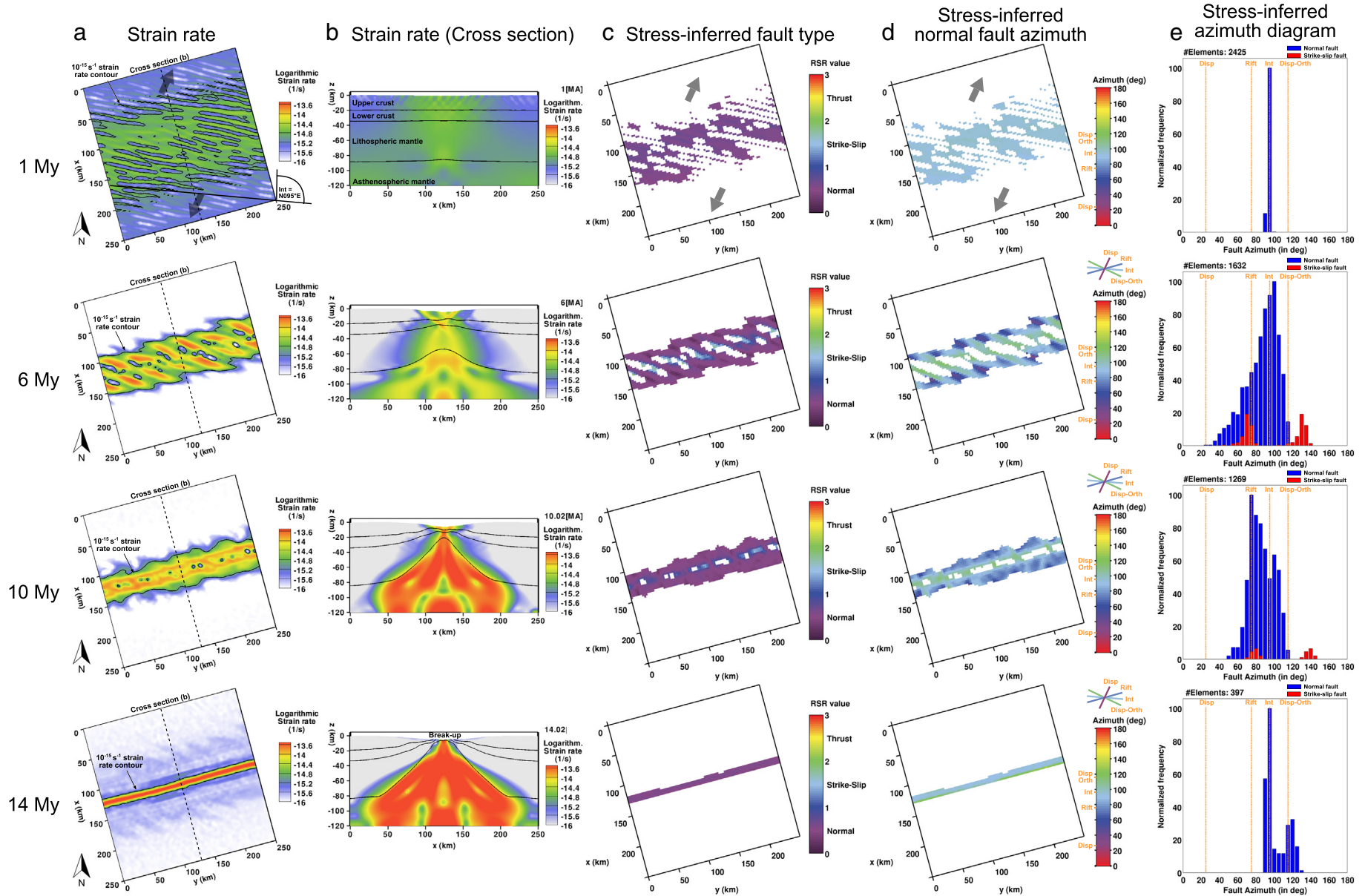
Fig. 3. Standard scenario evolution. Model evolution at 1 My, 6 My, 10 My, and 14 My (i.e. 10 km, 60 km, 100 km, and 140 km extension, respectively). (a) Surface strain rate pattern (shown is the second invariant of the strain rate tensor). Initially, shear zones are parallel to the expected intermediate azimuth of N095°E. At 6 My a complex en-echelon pattern occurs. (b) Mid-model strain rate cross section as shown in (a). Black lines indicate boundaries between material layers. Lithospheric necking and crustal faults localise toward the rift centre until break-up occurs at 14 My. (c) The stress tensor of each surface element is visualised in terms of stress regime. White areas experience negligible tectonic deformation (strain rate < 10^{-15} s^{-1}, see contour in (a)) and are excluded from the stress analysis. Normal faulting is the dominant mechanism except for a temporary strike-slip region in the rift centre. (d) In places where the stress regime indicates normal faulting, we plot the normal fault azimuth. The en-echelon pattern at 6 My strongly affects local stress orientations. (e) Frequency diagram of stress-inferred normal and strike-slip fault azimuths. The amplitude is normalized by the number of elements inside the tectonically active region (see contour in (a)). Note that figures showing the whole evolution in steps of 1 My can be found in the supplementary material.

Azimuth is measured as the clockwise angle from the northward direction.

In analogue experiments and field surveys, the relative importance of individual fault populations can be expressed in terms of cumulated fault length, whereas in our numerical model, we simply count the number of elements that belong to a specific azimuth range. In contrast to standard top-view interpretations of analogue models, our method allows to directly discriminate between strike-slip, normal, and thrust faults. For strike-slip faults, however, stress tensor information alone does not suffice to differentiate between dextral and sinistral conjugates. Hence, we depict the conjugate fault families in two different clusters that are scaled by a factor of 0.5 so that the overall number of evaluated elements is not affected.

The stress interpretation method allows to compute stress regime and fault azimuth for any stress tensor at the model surface, even though the considered element experiences no strain at all. Hence, it is necessary to exclude the quasi non-deforming elements outside the rift zone from the analysis. We therefore restrict our analysis to the zone of tectonic activity, where the strain rate exceeds 10^{-15} s^{-1}. This number is somewhat arbitrary, but the overall results are not affected if the threshold value is changed within reasonable range. This is due to the fact that the area of high tectonic surface activity becomes very well constrained shortly after model start (Fig. 3a). Note that the extent of the active region successively localises towards the rift centre. Therefore, the overall number of elements that experience high strain rate, and that contribute to the analysis, decreases with time. This number is indicated for each time step in the upper left corner of the azimuth diagram.

The fundamental assumption of this method is that the stress state dictates fault geometry. However, this is only true for homogeneous, isotropic media. In natural settings, inherited faults are common and reactivation may occur which may lead to non-Andersonian fault geometries. Moreover, the method accounts only for incremental faulting as no information on previous small-scale fault geometry is inherited to the next time step. In the strict sense, the assumption that one principal stress is oriented perpendicular to Earth's surface does not hold true if strong topographic gradients exist. This limitation should be remembered during stress interpretation at rift shoulders, although due to smooth topography variation in our model, local gradients are relatively small. Keeping these drawbacks in mind, it is one aim of this article to investigate the scope of this method by comparing its results to analogue experiments (Section 4) and the Gulf of Aden rift system (Section 5).

3. Numerical model results

3.1. General deformation pattern

The strain rate plots of Fig. 3a depict finite-width shear zones with a typical width of few elements. The spontaneous formation of shear zones takes place within the first computational time steps. Due to strain softening, shear zones become weaker with accumulated deformation so that individual small-scale shear zones compete and their number reduces with time.

The largest amount of deformation is taken up by shear zone parts atop the lithospheric necking domain. During the first 6 My, large conjugate normal faults develop within the shear zones that cut through the whole crust (Fig. 3b). During continued rifting, the distance of the conjugate faults at the surface is reduced with time until it vanishes and break-up takes place at 14 My. This model does not account for petrophysical formation of oceanic crust so that continental break-up is assumed to occur when the lithosphere is broken and asthenospheric material reaches the surface.

Three fault azimuths play a fundamental role during the discussion of the model, i.e. rift-parallel (N075°E), displacement-orthogonal (N115°E),

and intermediate (N095°E). We discuss the processes that underlie each direction in Section 5.3.

3.2. Three-phase evolution

The evolution of the numerical model can be divided in three main phases. Note, however, that the transitions between phases are not abrupt but take place over 1 or 2 My. Figures showing the evolution in steps of 1 My can be found in the electronic supplement.

3.2.1. Phase 1

(1–5 My): At 1 My, the strain rate pattern of Fig. 3a shows small-scale shear zones that strike N095°E, which is intermediate between the displacement-orthogonal direction and the rift orientation. Within few million years, they develop into an en-echelon system with a wavelength of several tens of kilometres. The stress regime (Fig. 3c), is of extensional type everywhere and shows optimal fault orientation with intermediate directions (Fig. 3d,e).

3.2.2. Phase 2

(6–13 My): Deformation of the en-echelon shear zones strongly localises towards the lithospheric necking region (Fig. 3a). The normal fault azimuth map (Fig. 3d) shows that the en-echelon structure features a complex stress pattern: At the rift border, rift-parallel faulting and intermediate normal faulting takes place. Simultaneously, strike-slip faults and displacement-orthogonal normal faults occur in the rift centre that delimit individual shear zones (Fig. 3c,d). The azimuth diagram shows a shift from intermediate to rift-parallel directions and even involves fault azimuths that are smaller than N075°E. At 10 My, rift-parallel faults are dominant at the rift borders and a strong localization of the deformation towards the rift centre reoccurs while the en-echelon pattern vanishes.

3.2.3. Phase 3

(14 My and after): Incipient break-up links the individual shear zones. Instead of multiple ridge segments that are offset by ridge-orthogonal fracture zones, our model produces a single straight ridge oblique to extensional direction. This mode of oblique sea-floor spreading is known from slow and ultra-slow mid-oceanic ridges (Montési and Behn, 2007) whereby our extension rate of 10 mm/yr satisfies the condition for ultra-slow spreading (<12 mm/yr, Dick et al., 2003). However, the tendency of the system to produce the rectangular ridge-transform spreading pattern can be seen in the stress-inferred azimuth diagram (Fig. 3e at 14 My), where displacement-orthogonal faults are visible together with intermediate fault directions during break-up of the lithosphere.

The final strain distribution (Fig. 4a at 14 My) shows sigmoid deformation patterns. The sigmoidal shape can be explained by successive rift localisation and the longevity of individual shear zones: After formation of the initial en-echelon pattern, the central portion of each shear zone gets stretched parallel to the direction of extension which appears as a clockwise rotation (Fig. 4b). Since deformation localises towards the rift centre, the area where rotation occurs narrows with time. Thus, shear zones in the proximal margin experience less rotation while distal margin shear zones are deformed until they are nearly parallel to the direction of extension.

3.3. Alternative model setups and robustness of results

In this section we study the robustness of our results. We therefore change the initial configuration of the model by (i) decreasing and (ii) increasing the depth of the lithosphere–asthenosphere boundary followed by (iii) a model run with two times coarser numerical resolution.

Changing the LAB depth severely affects the initial strength distribution through the vertical temperature profile at model start: A shallow
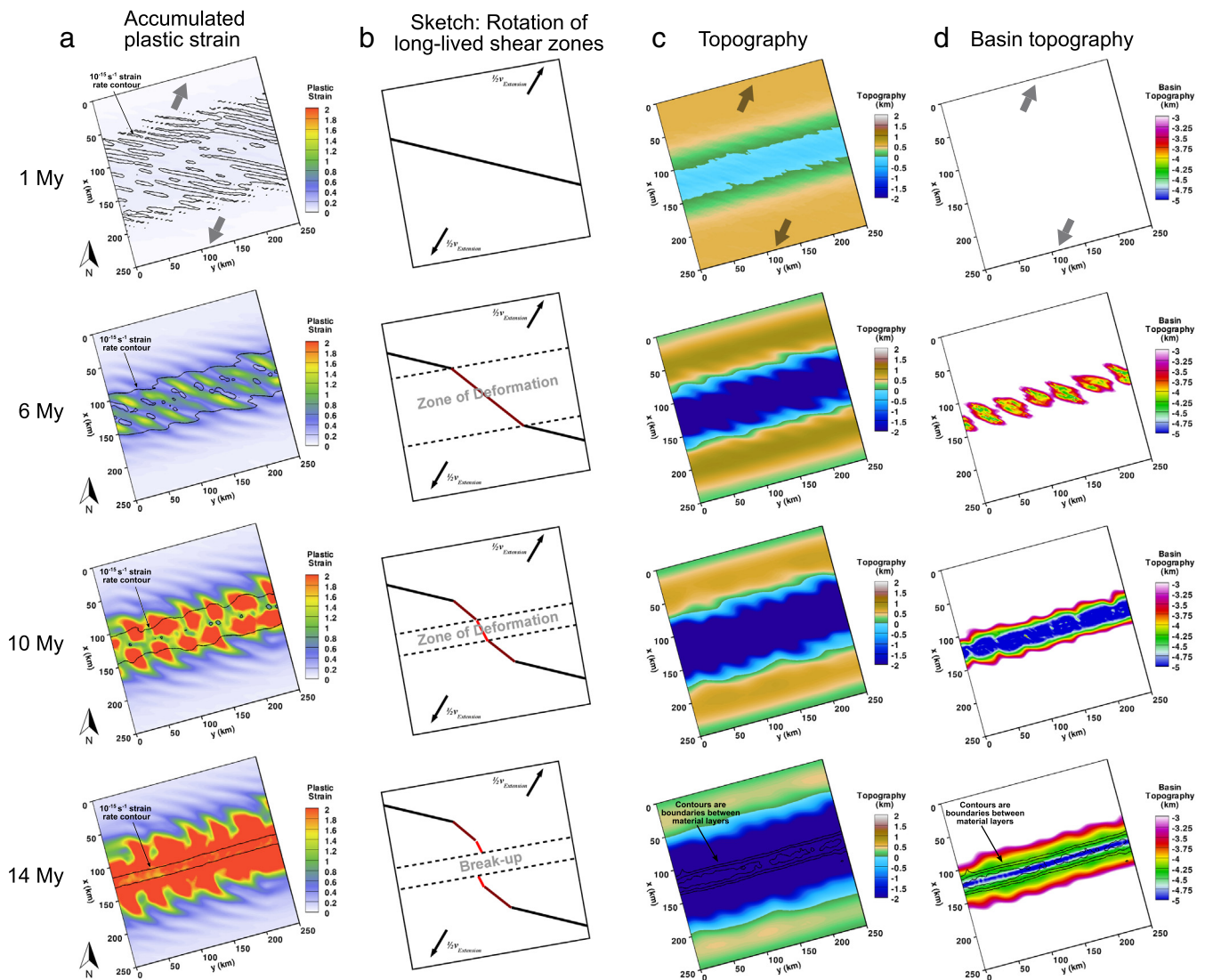
Fig. 4. Strain and topography patterns of the standard scenario. (a) The accumulated plastic strain shows formation of sigmoidal deformation patterns. The active region is outlined by the strain rate contour. (b) Illustration of how long-lived shear zones generate sigmoidal strain patterns. (c) Topography shows rift shoulder uplift due to hot asthenospheric upwelling at 6 My followed by subsidence due to lithospheric cooling. (d) The geometry of the basins is controlled by shear zone location and wavelength. Note that figures showing the whole evolution in steps of 1 My can be found in the supplementary material.

thermal LAB of 80 km (instead of the previously used 100 km) results in a weak mantle lithosphere and involves less brittle deformation within the crust (Fig. 2c). On the contrary, a thick lithosphere of 120 km produces both strong crust and mantle (Fig. 2d). In that case, crustal deformation is dominated by brittle failure. In both scenarios, we initiate the chemical LAB (i.e. the boundary between dry and wet olivine rheologies) 10 km above the thermal LAB.

Initially, the model with 80 km deep thermal LAB does not involve localised shear zones as in the previous simulation: At 1 My, the strain rate is much more distributed both at the surface (Fig. 5a) and in depth (Fig. 5b). This is due to the fact that the viscously deforming crustal domain is much thicker than the brittle portions of the crust. Consequently, brittle strain softening is less efficient in focussing deformation into discrete shear zones. After 15 My, a wide necking zone evolves and individual shear zones emerge with intermediate (N095°) orientations that are visible both in surface strain rate (Fig. 5a) and stress-inferred fault azimuth (Fig. 5d,e). These shear zones successively merge into two large zones of deformation that are oriented in a displacement-orthogonal direction. Individual segments of the shear zones with a specific orientation display the respective normal fault azimuth (Fig. 5d at 25 My): Displacement-orthogonal parts, for

example, show displacement-orthogonal fault orientations. During break-up at 25 My, the surface shear zones strongly resembles offset mid-ocean ridge segments. Note that these displacement-orthogonal ridges occur in the thin-lithosphere model but not in the standard scenario. The cause probably lies in the relationship between plate strength and ridge segment lengths. If plates are strong, mid-oceanic ridge segments are long, whereas weak plates with low effective viscosity generate short segments (Gerya, 2010 and references therein). Thus, the setup with hotter and hence weaker lithosphere can produce smaller ridge segments that fit into the modelling domain, while a larger model size would be needed to observe segmentation in the standard scenario.

The model with a 120 km thick lithosphere is strongly controlled by brittle localisation (Fig. 6). The overall evolution is similar to the standard scenario with a 100 km deep thermal LAB, although brittle localisation plays a stronger role. At 1 My, distinct parallel shear zones interconnect at depth in a highly symmetric fault network (Fig. 6a,b). Deformation localises into the rift centre and forms several large shear zones that interconnect via en-echelon pattern. Simultaneously, the stress-inferred fault azimuth shifts towards a rift-parallel orientation while strike-slip domains emerge between the shear zones. The overall azimuth pattern shows a higher complexity than the standard scenario
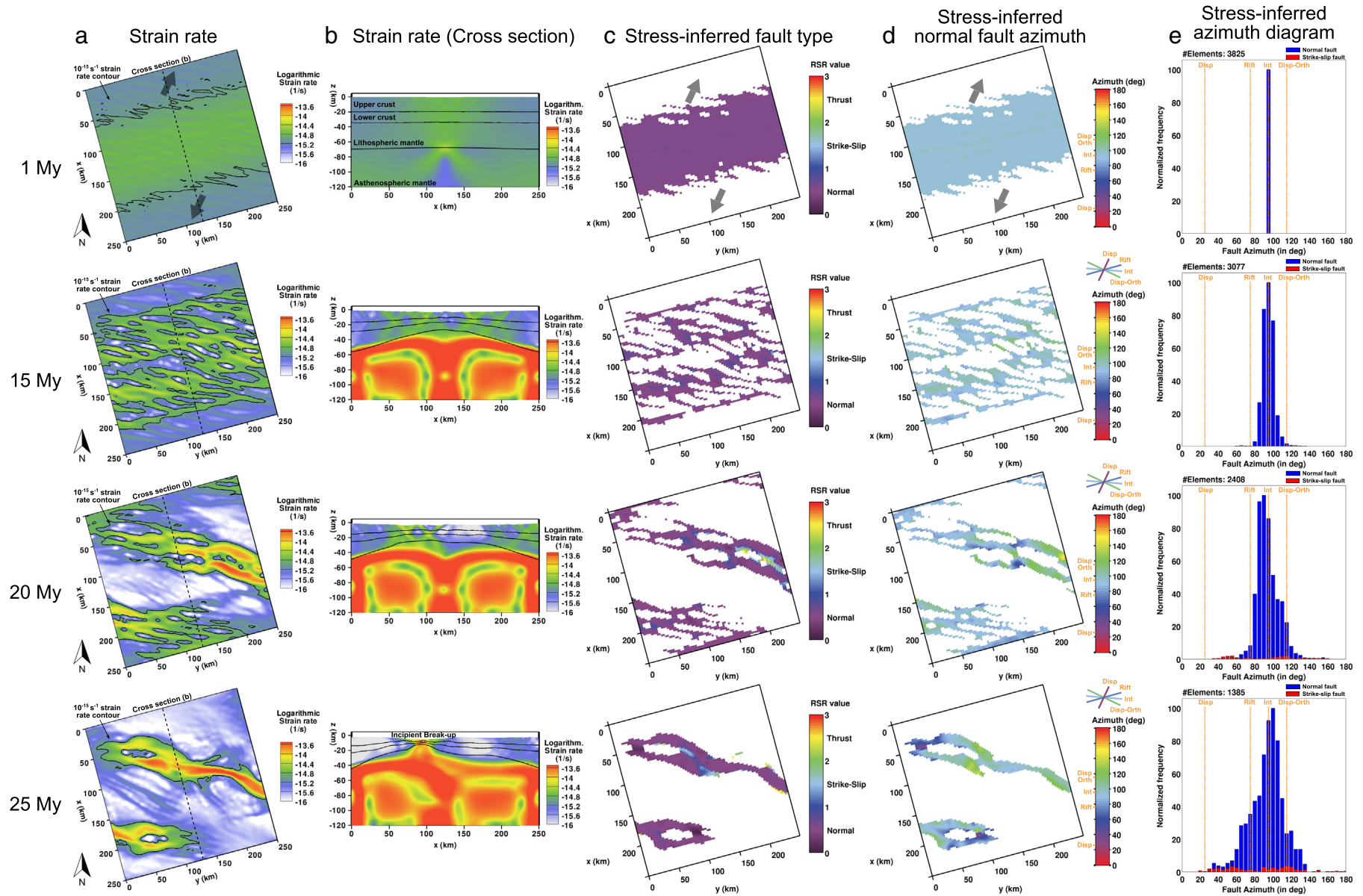
Fig. 5. Alternative setup with thin lithosphere (80 km). The initial strength distribution of this scenario is shown in Fig. 2c. Viscous rheology dominates the rift system and significantly prolongs the rift process, so that break-up takes place 10 My later than in the standard scenario. Described phases of the standard scenario are not applicable to this model. Localisation proceeds without en-echelon pattern towards large displacement-orthogonal structures (20 and 25 My). Normal fault azimuths involve rift-parallel, intermediate and displacement-orthogonal directions.

ARTICLE IN PRESS
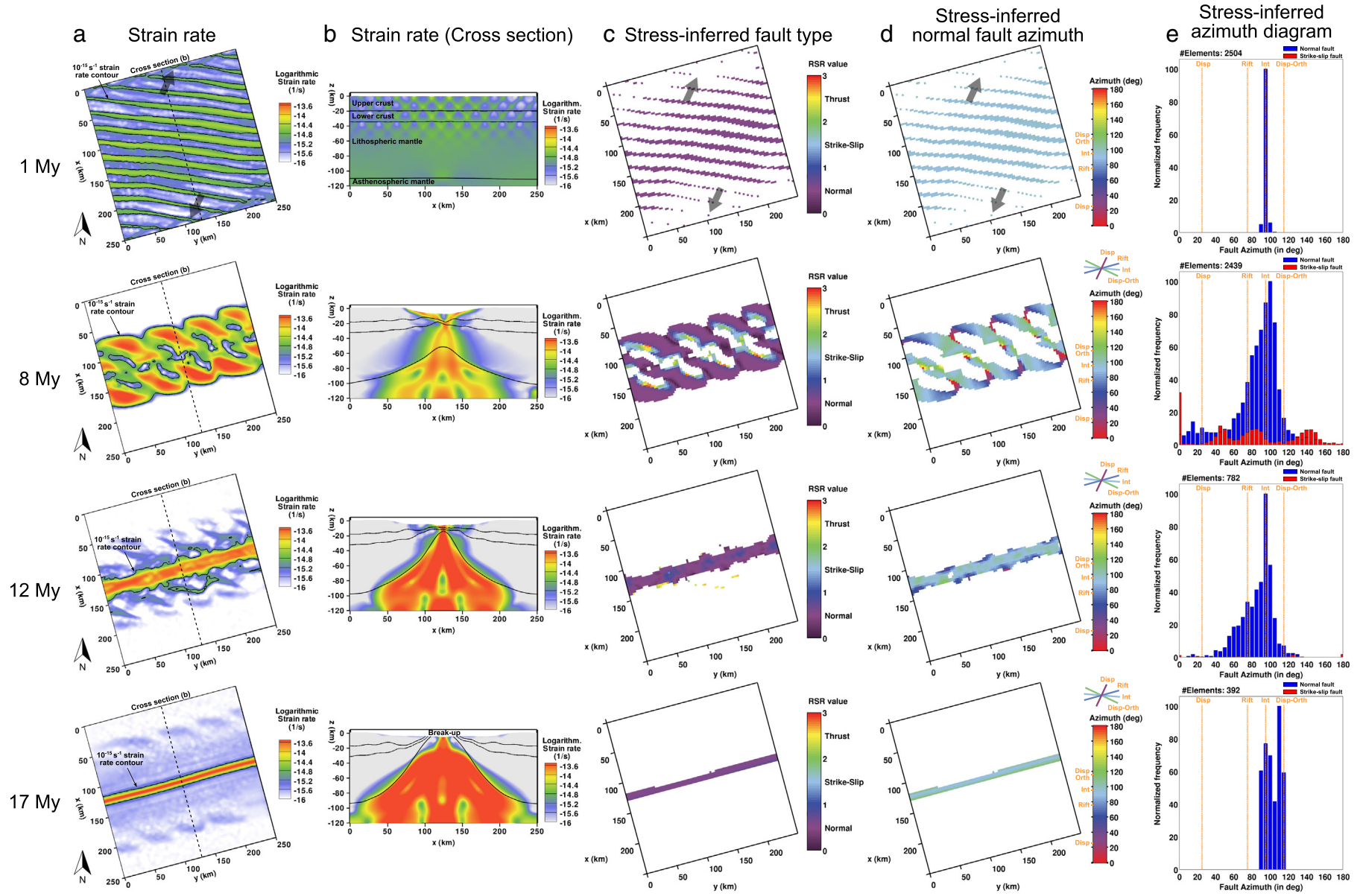
Fig. 6. Alternative setup with thick lithosphere (120 km). The initial strength distribution of this scenario is shown in Fig. 2d. Although crustal faulting is much more pronounced than in the standard scenario, overall rift evolution involves the described three phases. Stress rotations in the en-echelon zone at 8 My are more complex than in the standard model systematically involving all possible fault directions.
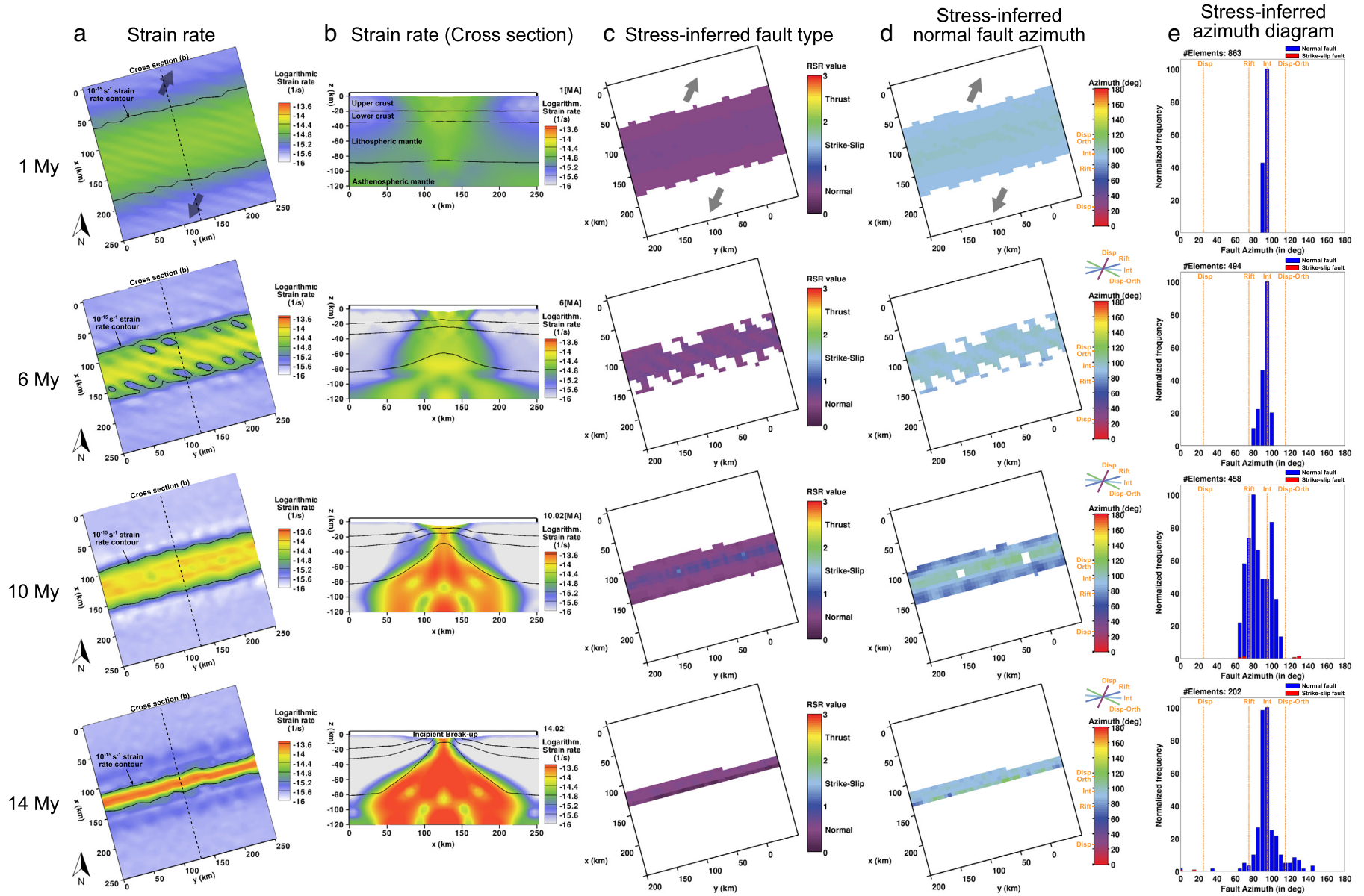
Fig. 7. Low-resolution model (6 km element size, instead of 3 km). Although distinct shear zones are more diffuse than in the standard scenario (Fig. 3), the overall model evolution is very similar in terms of timing, deformational structures and normal fault orientations.
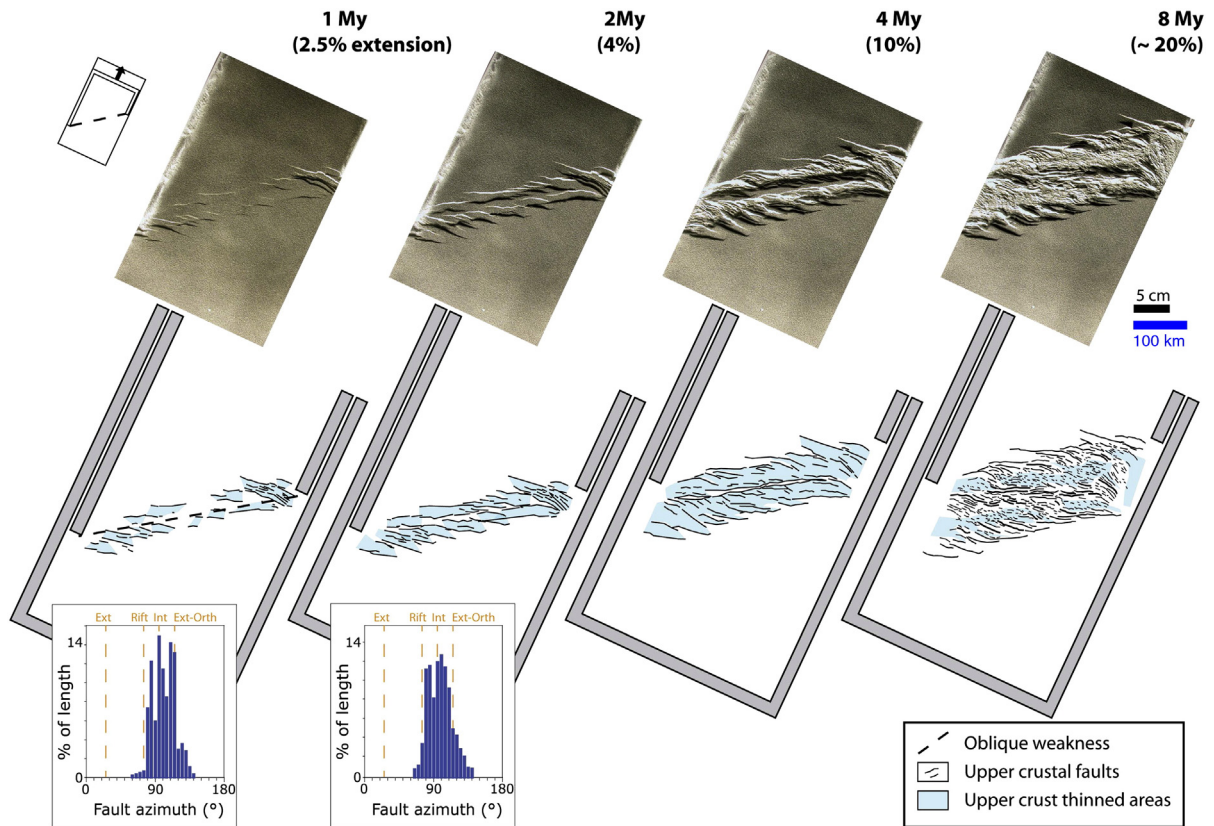
Fig. 8. Analogue model evolution. Top view photographs and interpretations of the lithosphere-scale analogue model with four brittle and ductile layers. In agreement with the numerical model, the analogue model evolves in distinct phases whereby rift-parallel orientations occur at the rift flanks while intermediate and displacement-orthogonal fault directions dominate the rift centre.

incorporating all possible fault orientations. During break-up all strains are taken up by a single straight shear zone in the model centre and the stress-inferred fault diagram indicates intermediate and displacement-orthogonal fault azimuths. The spacing between individual shear zones and the width of associated basins results from a dynamic interplay involving the brittle–ductile transition depth in the upper crust (e.g. Vendeville et al., 1987), the strength contrast between upper and lower crust (Wijns et al., 2005) and the lithospheric necking width. For example, the deeper brittle–ductile transition depth in the thick-lithosphere model at 1 My and 8 My (Fig. 6) allows to accommodate less shear zones than the standard scenario (Fig. 3) so that specific basins must have a larger wavelength.

In order to evaluate the influence of model resolution on our results, we modify the standard scenario by two times coarser resolution (i.e. 6 km element length instead of 3 km, Fig. 7). The overall rift evolution is similar to that of the original model. Although the shear zones are more diffuse both in map view and cross section, both the necking width and general timing correspond very well. Strong similarity exists in variables that have been inferred through the stress-interpretation technique: We find predominantly normal faulting with intermediate orientation in Phase 1, a strong tendency towards rift-parallel faulting during Phase 2 and intermediate to displacement-orthogonal azimuths upon break-up. Differences with respect to the standard model involve the less well expressed strike-slip populations during phase 2 and that displacement-orthogonal azimuths are less expressed during break-up. In quintessence, this experiment shows that the overall model evolution is relatively independent of model resolution. Moreover, we argue that stress-inferred variables allow resolution-independent conclusions.

3.4. Model limitations

Note that the model capabilities are limited in several aspects. Most importantly, magma migration and dike formation that tend to decrease lithospheric strength perpendicular to the direction of extension are not accounted for. Surface processes like erosion and sedimentation are not included. Besides, the limits of computational power restrict our model resolution to 3 km which is still far from resolving individual faults. Nevertheless, the presented model is one of the first to reproduce lithospheric-scale rift evolution from initial deformation until break-up.

4. Numerical model vs. Gulf of Aden analogue model

Before we compare the numerical model to the Gulf of Aden, we will explore differences and similarities to the previously conducted lithospheric-scale analogue model of Autin et al. (2010) that also featured an obliquity of 40°. As the numerical model uses a prescribed weakness in the lithosphere, we compare it to an analogue experiment which also contains a pre-existing lithospheric weakness (Fig. 8).

The analogue model is constructed in order to reproduce oblique rifting by way of shifted lateral velocity discontinuities (see Autin et al., 2010 for details). Moreover, an oblique weakness trends parallel to the direction of obliquity imposed by the lateral velocity discontinuities, and joins them. The model involves a four-layer type lithosphere strength profile (shown in Fig. 2e) modelled using granular materials and silicone. This modelled lithosphere overlies a low viscosity, higher density glucose syrup that mimics the asthenosphere. Lateral dimensions of the setup (56 cm times 30 cm in the laboratory) scale to

750 km times 400 km in reality. The maximum extension of the model is 20% which corresponds to 80 km if scaled to natural dimensions or to 8 My of our numerical model evolution.

Autin et al. (2010) also observed the three main fault populations: Rift-parallel, intermediate, and displacement-orthogonal. Moreover, the proposed three steps of development are very similar to the ones observed in the numerical models (Fig. 8): (i) The fault populations, especially during the early stages of deformation, are composed of intermediate faults. This fault population is characteristic for oblique rifts as observed in previous studies. (ii) In later stages, faults parallel to the rift become numerous and are located in the rift borders where thinning is most important. (iii) During the final stages of extension, the small-scale deformation pattern is composed of displacement-orthogonal faults in the deepest parts, i.e. in the rift centre.

Although the three stages are similar to the ones observed in the numerical models, several differences exist: The numerical model indicates that during the Phase 1, only intermediate faults develop, whereas in the analogue model, also displacement-orthogonal faults develop. However, these orientations occur near the model boundary and may hence be related to boundary effects. Phase 3 of the numerical model displays displacement-orthogonal as well as intermediate faults (Fig. 3d), whereas Autin et al. (2010) infer that only displacement-orthogonal faults form in the analogue models at this stage. Unfortunately, the advanced deformation inhibited precise measurements of the fault lineaments and no statistic plot is available for this stage. In the numerical model, this stage is controlled by the ascent of the hot asthenosphere and subsequent plate cooling, which cannot be reproduced in analogue models. These processes induce a strong localization of the deformation, where oblique weakening combined with the far-field stress could lead to intermediate fault development. The azimuth diagram (Fig. 3e) shows clearly displacement-orthogonal faults at 14 My, when the break-up occurs. This is different from the analogue model, which suggests that they appear at earlier stages. It is noteworthy that clockwise rotations of the structural pattern start at 7 My in the numerical model. Rotations are observed in the analogue models and result in the same general sigmoid pattern.

Another fundamental similarity between the models is the location of faults with similar azimuth. In the numerical as well as the analogue models, rift-parallel faults are always located along the rift flanks. This is where the overall oblique thinning of the lithosphere creates a strong lateral density contrast between the dense lithosphere and the hot ascendant asthenosphere. These variations are thought to induce an extensional force component perpendicular to the rift flanks (Bellahsen et al., this volume). On the contrary, displacement-orthogonal faults are always created in the rift centre where the lateral density contrast is much smaller.

5. Numerical model vs. Gulf of Aden natural rift

5.1. Chronology and localisation of the fault populations

First we compare the distribution of the fault populations in the rift and their chronology. As described in Bellahsen et al. (this volume), the Gulf of Aden displays a systematic fault organisation (Fig. 1): (i) The external parts of the rift show intermediate and displacement-orthogonal faults; (ii) the rift borders focus rift-parallel faults and; (iii) the internal parts are mainly composed of intermediate fault in the OCT and displacement-orthogonal faults close to the mid-oceanic ridge. If we consider that the deformation localises progressively towards the rift centre (e.g. Corti et al., 2003; Ring et al., 1992), then the structures of the proximal margin should be older than those of the distal one. This evolution is in accordance with the 3 step evolution of the numerical model. Indeed, Fig. 3d,e shows that (i) the intermediate faults are created first and will then be located in the external parts of the rifts; (ii) rift-parallel faults form later and are localised at the rift borders where lithospheric thinning is strongest, i.e. at 100 km and 150 km along the *x*-axis at 6 My or

110 km and 140 km at 10 My; and (iii) intermediate and displacement-orthogonal faults appear in the rift centre during the final evolution of the model.

The numerical model reproduces the actual Gulf of Aden rift duration of 14 My from initial localisation to final break-up (Leroy et al., 2012). The temporal fault kinematic history of the Gulf of Aden rift system is presently still speculative. We therefore propose that the timing of our model's rift phases can be indicative for future kinematic studies of the evolution of faults in the Gulf of Aden.

5.2. Final deformation pattern

The overall deformation pattern of the Gulf shows an en-echelon arrangement of the syn-rift faults and grabens, on both sides of the oblique OCT (Fig. 1a). When the Gulf is closed to the OCT (Fig. 1b), the main Tertiary depocentres show en-echelon sigmoid grabens. This pattern is similar to the plastic strain pattern observed in the numerical model (Fig. 4a). The modelled basin topography is also comparable with en-echelon sigmoid basins that became progressively linked and that separated when the final localization occurred at 10–11 My (Fig. 4d). Nevertheless, this en-echelon deformation occurs at larger scale (ca. 100 km) than in the numerical model (40–50 km) and is partly controlled by the Mesozoic inheritance (Autin et al., this volume; Ellis et al., 1996; Granath, 2001; Leroy et al., 2012). The difference in wavelength is certainly due to the initial pattern of the inherited, widely spaced Mesozoic basins, which have focused the deformation during their reactivation, preventing the appearance of a more distributed pattern as in the numerical model. Although the main Tertiary depocentres focus in these inherited basins, deformation is also observed outside of them as for example in the Ashawq graben. Thus, it appears that the distributed deformation pattern of the model can be recognised in the Gulf of Aden but is locally controlled and enhanced by the inheritance that overprinted the general pattern.

As proposed above, the sigmoidal shape in the model can be due to successive rotations during ongoing extension of long-lived shear zones (Fig. 4b). In the Gulf of Aden, the inherited Mesozoic basins have a sigmoidal shape and thus could have experienced such rotations. Novel analogue models that reproduce this inheritance during oblique rifting show indeed that the inherited structure ends with a sigmoid shape (Autin et al., this volume).

5.3. Processes that control major fault orientations

The intermediate fault direction (N095°E) plays a prominent role during all three phases of the model. The underlying reason for the occurrence of this orientation is the combined effect of both extensional far field stresses and its local modification by the rift zone as proposed by Withjack and Jamison (1986).

During Phase 2 (6 to 13 My), the progressive development of rift-parallel faults indicates that deformation localises along the oblique trend. The rift-parallel fault orientation can be linked to necking-related buoyancy forces that generate a rift-orthogonal stress component (Bellahsen et al., this volume): These buoyancy forces can be caused by thickness variations in the lithosphere producing lateral density variations between the dense lithosphere and the less dense, hotter ascendant asthenosphere so that the resulting force direction is perpendicular to the major lithosphere thinning (e.g. Artyushkov, 1973; Fleitout and Froidevaux, 1982). This hypothesis is supported by the localisation of rift-parallel faults in the rift borders above the maximal gradient of lithosphere thickness (Fig. 3b,d). Additionally, necking-related buoyancy has been considered an important driving force for rifting evolution even in orthogonal, 2D rift settings (Burov, 2007; Davis and Kusznir, 2002; Huismans et al., 2001). An alternative reason for rift-parallel faulting is strain partitioning between rift centre and rift flanks: Strike-slip faults emerge in the rift centre (Fig. 3c) at the same time as rift-parallel faulting occurs at the rift borders. The strike-slip zone

partly accommodates the rift-parallel component of extension so that rift flanks experience only the rift-perpendicular velocity component which induces the observed rift-parallel fault direction. Strain partitioning has been observed in both natural rift systems like the Main Ethiopian Rift and corresponding analogue experiments (Agostini et al., 2011).

Deformation during the third step (from 14 My on) is localised in the rift centre. The intermediate and displacement-orthogonal faults indicate that the far-field extension dominates. The rift centre is far enough from the thinning zones (rift borders) so that the newly formed faults develop mainly in response to the far field stresses, as proposed in Autin et al. (2010). Nevertheless, the presence of intermediate faults suggests that a local stress field is still active. The reason is probably that plate cooling takes place perpendicular to the oblique rift zone. The ongoing evolution of the model shows that intermediate fault proportion tends to decrease with time compared to the displacement-orthogonal faults, suggesting that the far-field is more and more dominant.

6. Conclusion

The proposed stress interpretation method intuitively visualises the surface stress field in terms of stress regime and optimal fault orientation. It allows to extract significantly more details of the model evolution than mere interpretation of strain-rate and strain fields. A comparison with analogue models and the natural Gulf of Aden shows very good agreement in many aspects. We stress that this method can be easily introduced in the post-processing step of any numerical geodynamic model.

We identify a characteristic three-phase evolution of fault patterns. Phase 1 (1-5 My): Faults develop with orientations that are intermediate between the rift-direction and the displacement-orthogonal. Phase 2 (6–13 My): Rift-parallel normal faults occur at the rift flanks simultaneously with strike-slip faults and displacement-orthogonal faults in the central part of the rift system. Phase 3 (after 13 My): Displacement-orthogonal as well as intermediate orientation dominate during break-up and thereafter.

We relate these steps to the following deformation processes: (i) Interaction of the far-field stress and the local stresses induced by the weakness zone generates intermediate faults. (ii) Necking-related buoyancy forces affect the local stress field and create rift-parallel faults. Additionally, strain partitioning between the rift centre and the rift flanks generates rift-parallel fault orientations at the rift borders. (iii) During break-up, far-field stress conditions become progressively important, creating intermediate and displacement-orthogonal faults.

Acknowledgements

Appendix A. Supplementary data

Supplementary data to this article can be found online at http://dx.doi.org/10.1016/j.tecto.2013.06.029.

References

Agostini, A., Corti, G., Zeoli, A., Mulugeta, G., 2009. Evolution, pattern and partitioning of deformation during oblique continental rifting: Inferences from lithospheric-scale centrifuge models. Geochemistry, Geophysics, Geosystems 10, Q11015. http://dx.doi.org/10.1029/2009GC002676.

Agostini, A., Bonini, M., Corti, G., Sani, F., Mazzarini, F., 2011. Fault architecture in the Main Ethiopian Rift and comparison with experimental models: implications for rift evolution and Nubia–Somalia kinematics. Earth and Planetary Science Letters 301, 479–492.

Allken, V., Huismans, R.S., Thieulot, C., 2011. Three-dimensional numerical modeling of upper crustal extensional systems. Journal of Geophysical Research 116, B10409. http://dx.doi.org/10.1029/2011JB008319.

Allken, V., Huismans, R.S., Thieulot, C., 2012. Factors controlling the mode of rift interaction in brittle–ductile coupled systems: a 3D numerical study. Geochemistry, Geophysics, Geosystems 13 (5), Q05010. http://dx.doi.org/10.1029/2012GC004077.

Anderson, E.M., 1948. The Dynamics of Faulting. Oliver and Boyd, Edinburgh and London.

Artyushkov, E.V., 1973. Stresses in the lithosphere caused by crustal thickness inhomogeneities. Journal of Geophysical Research 78 (32), 7675–7708. http://dx.doi.org/10.1029/JB078i032p07675.

Autin, J., Bellahsen, N., Husson, L., Beslier, M., Leroy, S., d'Acremont, E., 2010. Analogue models of oblique rifting in a cold lithosphere. Tectonics 29, TC6016. http://dx.doi.org/10.1029/2010TC002671.

Autin, J., Bellahsen, N., Leroy, S., Husson, L., Beslier, M.-O., d'Acremont, E., 2013. The role of structural inheritance in oblique rifting: insights from analogue models and application to the Gulf of Aden. http://dx.doi.org/10.1016/j.tecto.2013.05.041 (this volume).

Bassi, G., 1991. Factors controlling the style of continental rifting: insights from numerical modelling. Earth and Planetary Science Letters 105, 430–452.

Behn, M.D., Lin, J., Zuber, M.T., 2002. A continuum mechanics model for normal faulting using a strain-rate softening rheology: implications for thermal and rheological controls on continental and oceanic rifting. Earth and Planetary Science Letters 202, 725–740.

Bellahsen, N., Faccenna, C., Funiciello, F., Daniel, J., Jolivet, L., 2003. Why did Arabia separate from Africa? Insights from 3-D laboratory experiments. Earth and Planetary Science Letters 216, 365–381.

Bellahsen, N., Fournier, M., d'Acremont, E., Leroy, S., Daniel, J.M., 2006. Fault reactivation and rift localization: Northeastern Gulf of Aden margin. Tectonics 25, TC1007.

Bellahsen, N., Husson, L., Autin, J., Leroy, S., d' Acremont, E., 2013. The effect of thermal weakening and buoyancy forces on rift localization: field evidences from the Gulf of Aden oblique rifting. Tectonophysics (Special Issue: The Gulf of Aden rift). http://dx.doi.org/10.1016/j.tecto.2013.05.042 (this volume).

Bosworth, W., Huchon, P., McClay, K., 2005. The Red Sea and Gulf of Aden basins. Journal of African Earth Sciences 43, 334–378.

Bott, M.H.T., 1959. The mechanics of oblique slip faulting. Geological Magazine 96 (2), 109–117.

Braun, J., Beaumont, C., 1989. A physical explanation of the relation between flank uplifts and the breakup unconformity at rifted continental margins. Geology 17, 760–764.

Brune, S., Popov, A.A., Sobolev, S.V., 2012. Modeling suggests that oblique extension facilitates rifting and continental break-up. Journal of Geophysical Research 117, B08402. http://dx.doi.org/10.1029/2011JB008860.

Brune, S., Popov, A.A., Sobolev, S.V., 2013. Quantifying the thermo-mechanical impact of plume arrival on continental break-up. Tectonophysics. http://dx.doi.org/10.1016/j.tecto.2013.02.009 (in press).

Buchmann, T.J., Connolly, P.T., 2007. Contemporary kinematics of the Upper Rhine Graben: a 3D finite element approach. Global and Planetary Change 58 (1–4), 287–309. http://dx.doi.org/10.1016/j.gloplacha.2007.02.012.

Buck, W.R., 1991. Modes of continental lithospheric extension. Journal of Geophysical Research 96, 20161–20178.

Buiter, S.J.H., Huismans, R.S., Beaumont, C., 2008. Dissipation analysis as a guide to mode selection during crustal extension and implications for the styles of sedimentary basins. Journal of Geophysical Research 113, B06406. http://dx.doi.org/10.1029/2007JB005272.

Burov, E., 2007. The role of gravitational instabilities, density structure and extension rate in the evolution of continental margins. In: Karner, G.D., Manatschal, G., Pinheiro, L.M. (Eds.), Imaging, Mapping and Modelling Continental Lithosphere Extension and Breakup. Geological Society, London, Special Publications, 282, pp. 139–156. http://dx.doi.org/10.1144/SP282.7.

Burov, E., Cloetingh, S., 1997. Erosion and rift dynamics: new thermomechanical aspects of post-rift evolution of extensional basins. Earth and Planetary Science Letters 150, 7–26.

Clifton, A.E., Schlische, R.W., Withjack, M.O., Ackermann, R.V., 2000. Influence of rift obliquity on fault-population systematics: results of experimental clay models. Journal of Structural Geology 22, 1491–1509. http://dx.doi.org/10.1016/S0191-8141(00)00043-2.

Corti, G., 2004. Centrifuge modelling of the influence of crustal fabrics on the development of transfer zones: insights into the mechanics of continental rifting architecture. Tectonophysics 384 (1–4), 191–208. http://dx.doi.org/10.1016/j.tecto.2004.03.014.

Corti, G., Bonini, M., Innocenti, F., Manetti, P., Mulugeta, G., 2001. Centrifuge models simulating magma emplacement during oblique rifting. Journal of Geodynamics 31 (5), 557–576. http://dx.doi.org/10.1016/S0264-3707(01).

Corti, G., Bonini, M., Conticelli, S., Innocenti, F., Manetti, P., Sokoutis, D., 2003. Analogue modelling of continental extension: a review focused on the relations between the patterns of deformation and the presence of magma. Earth-Science Reviews 63 (3–4), 169–247. http://dx.doi.org/10.1016/S0012-8252 (03)00035-7.

d'Acremont, E., Leroy, S., Beslier, M.-O., Bellahsen, N., Fournier, M., Robin, C., Maia, M., Gente, P., 2005. Structure and evolution of the eastern Gulf of Aden conjugate margins from seismic reflection data. Geophysical Journal International 160, 869–890.

Dauteuil, O., Huchon, P., Quemeneur, F., Souriot, T., 2001. Propagation of an oblique spreading center: the western Gulf of Aden. Tectonophysics 332, 423–442.

Davis, M., Kusznir, N., 2002. Are buoyancy forces important during the formation of rifted margins? Geophysical Journal International 149, 524–533.

Dick, H.J.B., Lin, J., Schouten, H., 2003. An ultraslow-spreading class of ocean ridge. Nature 426, 405–412.

Dunbar, J.A., Sawyer, D.S., 1996. Three-dimensional dynamical model of continental rift propagation and margin plateau formation. Journal of Geophysical Research 101, 27845–27863.

Ellis, A.C., Kerr, H.M., Cornwell, C.P., Williams, D.O., 1996. A tectono-stratigraphic framework for Yemen and its implications for hydrocarbon potential. Petroleum Geoscience 2, 29–42.

England, P., McKenzie, D., 1982. A thin viscous sheet model for continental deformation. Geophysical Journal of the Royal Astronomical Society 70, 295–321.

Fleitout, L., Froidevaux, C., 1982. Tectonics and topography for a lithosphere containing density heterogeneities. Tectonics 1 (1), 21–56. http://dx.doi.org/10.1029/TC001i001p00021.

Fournier, M., Bellahsen, N., Fabbri, O., Gunnell, Y., 2004. Oblique rifting and segmentation of the NE Gulf of Aden passive margin. Geochemistry, Geophysics, Geosystems 5.

Fournier, M., Huchon, P., Khanbari, K., Leroy, S., 2007. Segmentation and along-strike asymmetry of the passive margin in Socotra, eastern Gulf of Aden: are they controlled by detachment faults? Geochemistry, Geophysics, Geosystems 8.

Gac, S., Geoffroy, L., 2009. 3D thermo-mechanical modelling of a stretched continental lithosphere containing localized low-viscosity anomalies (the soft-point theory of plate break-up). Tectonophysics 468 (1–4), 158–168.

Gerya, T., 2009. Introduction to Numerical Geodynamic Modelling. Cambridge University Press.

Gerya, T., 2010. Dynamical instability produces transform faults at mid-ocean ridges. Science 329, 1047–1050.

Gleason, G.C., Tullis, J., 1995. A flow law for dislocation creep of quartz aggregates determined with the molten-salt cell. Tectonophysics 247, 1–23.

Granath, J.W., 2001. The Nogal Rift of Northern Somalia: Gulf of Aden. Reactivation of a Mesozoic Rift. Mémoires du Muséum national d'histoire naturelle, 186, pp. 511–527.

Hébert, H., Deplus, C., Huchon, P., Khanbari, K., Audin, L., 2001. Lithospheric structure of a nascent spreading ridge inferred from gravity data: the western Gulf of Aden. Journal of Geophysical Research 106 (B11), 26345–26363.

Hergert, T., Heidbach, O., 2011. Geomechanical model of the Marmara Sea region—II. 3-D contemporary background stress field. Geophysical Journal International 185, 1090–1102. http://dx.doi.org/10.1111/j.1365-246X.2011.04992.x.

Hirth, G., Kohlstedt, D., 2003. Rheology of the upper mantle and the mantle wedge: a view from the experimentalists. In: Eiler, J. (Ed.), Inside the Subduction Factory. Geophys. Monogr. Ser., vol. 138. AGU, Washington, D. C., pp. 83–105. http://dx.doi.org/10.1029/138GM06.

Houseman, G., England, P., 1986. Finite strain calculations of continental deformation: 1. Method and general results for convergent zones. Journal of Geophysical Research 91, 3651–3663.

Huchon, P., Khanbari, K., 2003. Rotation of the syn-rift stress field of the northern Gulf of Aden margin, Yemen. Tectonophysics 364, 147–166.

Huchon, P., Jestin, F., Cantagrel, J.M., Gaulier, J.M., Kirbash, S.A., Gafaneh, A., 1991. Extensional deformation in Yemen since Oligocene and the Africa–Arabia–Somalia triple junction. Annales Tectonicae 5, 141–163.

Huismans, R.S., Beaumont, C., 2003. Symmetric and asymmetric lithospheric extension: relative effects of frictional-plastic and viscous strain softening. Journal of Geophysical Research 108 (B10), 2496. http://dx.doi.org/10.1029/2002JB002026.

Huismans, R., Beaumont, C., 2011. Depth-dependent extension, two-stage breakup and cratonic underplating at rifted margins. Nature 473, 74–78.

Huismans, R.S., Podladchikov, Y.Y., Cloetingh, S., 2001. Transition from passive to active rifting: relative importance of asthenospheric doming and passive extension of the lithosphere. Journal of Geophysical Research 106, 11271–11291.

Kameyama, M., Yuen, D.A., Karato, S.I., 1999. Thermal-mechanical effects of low-temperature plasticity (the Peierls mechanism), on the deformation of a viscoelastic shear zone. Earth and Planetary Science Letters 168, 159–172.

Katzman, R., ten Brink, U.S., Lin, J., 1995. Three-dimensional modeling of pull-apart basins: implications for the tectonics of the Dead Sea Basin. Journal of Geophysical Research 100, 6295–6312.

Lavier, L.L., Manatschal, G., 2006. A mechanism to thin the continental lithosphere at magma-poor margins. Nature 440, 324–328.

Lavier, L.L., Buck, W.R., Poliakov, A.N.B., 2000. Factors controlling normal fault offset in an ideal brittle layer. Journal of Geophysical Research 105, 23431–23442.

Le Pourhiet, L., Huet, B., May, D.A., Labrousse, L., Jolivet, L., 2012. Kinematic interpretation of the 3D shapes of metamorphic core complexes. Geochemistry, Geophysics, Geosystems 13, Q09002. http://dx.doi.org/10.1029/2012GC004271.

Lepvrier, C., Fournier, M., Bérard, T., Roger, J., 2002. Cenozoic extension in coastal Dhofar (southern Oman): implications on the oblique rifting of the Gulf of Aden. Tectonophysics 357, 279–293.

Leroy, S., et al., 2010. Contrasted styles of rifting in the eastern Gulf of Aden: a combined wide-angle, multichannel seismic, and heat flow survey. Geochemistry, Geophysics, Geosystems 11 (Q07004), 1–14.

Leroy, S., et al., 2012. From rifting to oceanic spreading in the Gulf of Aden: a synthesis. Arabian Journal of Geosciences 5, 859–901.

Mart, Y., Dauteuil, O., 2000. Analogue experiments of propagation of oblique rifts. Tectonophysics 316, 121–132. http://dx.doi.org/10.1016/S0040-1951(99) (00231-0).

McClay, K.R., White, M.J., 1995. Analogue modelling of orthogonal and oblique rifting. Marine and Petroleum Geology 12 (2), 137–151. http://dx.doi.org/10.1016/0264-8172(95).

Melnick, D., Garcin, Y., Quinteros, J., Strecker, M.R., Olago, D., Tiercelin, J.J., 2012. Steady rifting in northern Kenya inferred from deformed Holocene lake shorelines of the Suguta and Turkana basins. Earth and Planetary Science Letters 331–332, 335–346.

Montési, L.G.J., Behn, M.D., 2007. Mantle flow and melting underneath oblique and ultraslow mid-ocean ridges. Geophysical Research Letters 34, 5.

Popov, A.A., Sobolev, S.V., 2008. SLIM3D: a tool for three-dimensional thermo mechanical modeling of lithospheric deformation with elasto-visco-plastic rheology. Physics of the Earth and Planetary Interiors 171, 55–75.

Popov, A.A., Sobolev, S.V., Zoback, M.D., 2012. Modeling evolution of the San Andreas Fault system in northern and central California. Geochemistry, Geophysics, Geosystems 13.

Quinteros, J., Sobolev, S.V., 2012. Constraining kinetics of metastable olivine in the Marianas slab from seismic observations and dynamic models. Tectonophysics 526–529, 48–55.

Quinteros, J., Sobolev, S.V., 2013. Why has the Nazca plate slowed since the Neogene? Geology 41 (1), 31–34.

Quinteros, J., Sobolev, S.V., Popov, A.A., 2010. Viscosity in transition zone and lower mantle: implications for slab penetration. Geophysical Research Letters 37, L09307.

Regenauer-Lieb, K., Weinberg, R.F., Rosenbaum, G., 2006. The effect of energy feedbacks on continental strength. Nature 442, 67–70.

Rey, P.F., Houseman, G., 2006. Lithospheric scale gravitational flow: the impact of body forces on orogenic processes from Archaean to Phanerozoic. Geological Society, London, Special Publications 253, 153–167.

Rey, P.F., Teyssier, C., Kruckenberg, S.C., Whitney, D.L., 2011. Viscous collision in channel explains double domes in metamorphic core complexes. Geology 39, 387–390.

Ring, U., Betzler, C., Delvaux, D., 1992. Normal vs. strike-slip faulting during rift development in east Africa: the Malawi rift. Geology 20 (11), 1015–1018.

Simo, J.C., Hughes, T.J.R., 2000. Computational Inelasticity, 2nd ed. Springer-Verlag, New York.

Simpson, R.W., 1997. Quantifying Anderson's fault types. Journal of Geophysical Research 102 (B8), 17,909–17,919.

Sokoutis, D., Corti, G., Bonini, M., Pierre Brun, J., Cloetingh, S., Mauduit, T., Manetti, P., 2007. Modelling the extension of heterogeneous hot lithosphere. Tectonophysics 444 (1–4), 63–79. http://dx.doi.org/10.1016/j.tecto.2007.08.012.

Tamsett, D., Searle, R.C., 1988. Structure and development of the midocean ridge plate boundary in the Gulf of Aden: evidence from GLORIA side scan sonar. Journal of Geophysical Research 93 (B4), 3157–3178. http://dx.doi.org/10.1029/JB093iB04p03157.

Tommasi, A., Vauchez, A., 2001. Continental rifting parallel to ancient collisional belts: an effect of the mechanical anisotropy of the lithospheric mantle. Earth and Planetary Science Letters 185, 199–210.

Tron, V., Brun, J.P., 1991. Experiments on oblique rifting in brittle–ductile systems. Tectonophysics 188, 71–84. http://dx.doi.org/10.1016/0040-1951(91)90315-J.

van Wijk, J.W., 2005. Role of weak zone orientation in continental lithosphere extension. Geophysical Research Letters 32, L02303. http://dx.doi.org/10.1029/2004GL022192.

Van Wijk, J.W., Blackman, D.K., 2005. Dynamics of continental rift propagation: the end-member modes. Earth and Planetary Science Letters 229, 247–258.

Van Wijk, J.W., Cloetingh, S.A.P.L., 2002. Basin migration caused by slow lithospheric extension. Earth and Planetary Science Letters 198, 275–288.

Vendeville, B., Cobbold, P., Davy, P., Brun, J., Choukroune, P., 1987. Physical models of extensional tectonics at various scales. Faulting and Related Processes 2, 171.

Watremez, L., Leroy, S., Rouzo, S., d'Acremont, E., Unternehr, P., Ebinger, C., Lucazeau, F., Al-Lazki, A., 2011. The crustal structure of the north-eastern Gulf of Aden continental margin: insights from wide-angle seismic data. Geophysical Journal International 184 (2), 575–594. http://dx.doi.org/10.1111/j.1365-246X.2010.04881.x.

Wijns, C., Weinberg, R., Gessner, K., Moresi, L., 2005. Mode of crustal extension determined by rheological layering. Earth and Planetary Science Letters 236, 120–134.

Wilks, K.R., Carter, N.L., 1990. Rheology of some continental lower crustal rocks. Tectonophysics 182, 57–77.

Withjack, M.O., Jamison, W.R., 1986. Deformation produced by oblique rifting. Tectonophysics 126 (2–4), 99–124. http://dx.doi.org/10.1016/0040-1951(86)90222-2.

Ziegler, P.A., Cloetingh, S., 2004. Dynamic processes controlling evolution of rifted basins. Earth-Science Reviews 64, 1–50.

Zuber, M.T., Parmentier, E.M., 1986. Lithospheric necking: a dynamic model for rift morphology. Earth and Planetary Science Letters 77, 373–383.